Chapter 3

Proton acceleration from magnetized overdense plasmas

Proton acceleration by an ultra-intense short-pulse circularly polarized laser from an overdense plasma target in presence of an axial magnetic field has been investigated with the help of three dimensional (3D) particle-in-cell (PIC) simulations. A difference in the behaviour of the ponderomotive force is observed in case of a right circularly polarized (RCP) and a left circularly polarized (LCP) laser in presence of magnetic field due to the modification of dielectric constant of plasma caused by the cyclotron effects. Ponderomotive force gets enhanced in case of a RCP laser which enhances the hot electron generation at the target front side. These hot electrons on reaching the target rear side can accelerate protons via. target normal sheath acceleration (TNSA) mechanism. On the other hand, in case of a LCP laser, reverse cyclotron effects causes a suppression of the ponderomotive force at a short distance strengthening the laser piston which enhances the effect of radiation pressure. An axial magnetic field can thus help in achieving higher radiation pressure at the target front side which can lead to effective acceleration of protons via. radiation pressure acceleration (RPA) mechanism in case of a LCP laser. The gyration of protons around the axial magnetic field due to cyclotron effects causes a reduction in the transverse proton momentum which increases the beam collimation to some extent. The optimum thickness of the overdense plasma target is observed to be increased in presence of an axial magnetic field.

3.1 Background of the study

Cyclotron effects induced by a magnetic field can have a considerable effect on the dynamics of hot electrons generated in intense laser-plasma interactions. This can cause a change in the dielectric constant of the plasma which can have a dramatic effect on the acceleration of ions. Generation of ultra-strong magnetic fields has gained a lot of interest recently. Magnetic fields of the order of 100 T sustainable up to longer time duration can now be readily produced using conventional techniques [1, 2]. Higher strength fields operating at shorter timescales are also produced [3]. Huge magnetic fields of the order of 10^8 G are produced during the interaction of an intense ultrashort laser pulse with a solid target [4–7]. Magnetic fields of the order of kT can be produced experimentally in the interaction of kilo-Joule high power lasers with a capacitor-coil target [8, 9] which is significant for a number of applications such as inertial confinement fusion [10]. These magnetic fields have more impact on the high energy electron flow as they get nonlinearly saturated. Recently, the study of laser plasma interactions in presence of strong magnetic field has gained the interest of researchers. Hosokai et al. [11] have experimentally investigated the effect of an external static magnetic field on the electron beams generated by laser-wakefield acceleration. They have observed that the emittance and total charge of electron beams gets significantly enhanced on applying a static magnetic field directed along the axis of laser pulse propagation. The formation of solitons during the the interaction of an intense laser pulse with plasma in presence of a strong magnetic field has been studied [12–14]. Bulanov et al. [15] have presented an analytical description of the strongly nonlinear oscillations in magnetized plasmas which show that the magnetic field prevents closing of the cavity formed behind the laser pulse. Sharma and Tripathi [16] have observed that the self-focusing of an intense right circularly polarized Gaussian laser pulse increases significantly in presence of an axial static magnetic field. Sharma et al. [17] have studied the generation of high energetic ions from an overdense plasma target in presence of an axial magnetic field. They have reported that the polarization of the laser pulse has a remarkable effect on ion acceleration. Right circular polarization (RCP) and left circular polarization (LCP) has different effects on ion acceleration in presence of an axial magnetic field as the plasma dielectric constant gets changed due to cyclotron effects, which in

turn enhances or reduces the ponderomotive force. They have also reported that the optimum thickness of the foil is sensitive to the left and right circular polarization as well as the applied axial magnetic field.

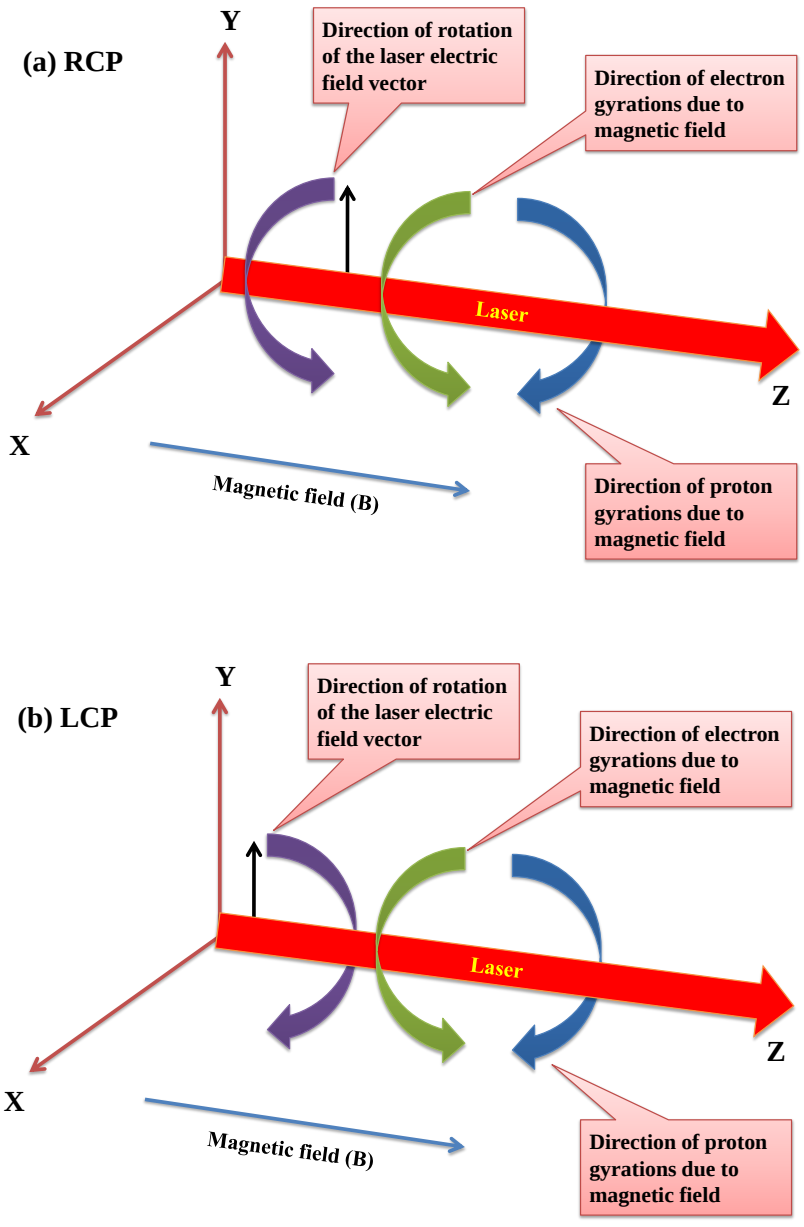

Fig. 3.1: Schematic diagram of the cyclotron effects in case of (a) RCP and (b) LCP.

Literature reveals that most of the phenomena related to laser plasma interactions in presence of magnetic field has been investigated analytically. In the present work, we investigate the acceleration of protons from an overdense plasma target in presence of an axial magnetic field with the help of 3D-PIC simulations using the code Picpsi-

3D [18]. RCP and LCP laser pulse have different effects on the plasma particles in presence of an axial magnetic field due to cyclotron effects. It is observed that the protons are accelerated more effectively by a LCP laser pulse, whereas the maximum proton energy gets reduced in case of RCP.

3.2 Electron dynamics induced by a circularly polarized laser in presence of an axial magnetic field

A RCP laser and a LCP laser act differently on electrons in presence of an axial magnetic field due to cyclotron effects. In case of a RCP laser, the direction of rotation of electrons by the laser electric field and the direction of electron gyrations by an axial magnetic field are same, which enhances the effect of the laser ponderomotive force. Hence, the electrons gain more energy in case of a RCP laser. On the other hand, in case of a LCP laser, the direction of electron rotations by the laser electric field and the axial magnetic field gyrations are opposite, which reverses the cyclotron effects as shown in Fig. 3.1. This opposes the electron motion and causes a reduction in the electron energy. Thus, the electrons move longer distances on gaining higher energy in case of a RCP laser. Whereas, in case of a LCP laser, the electrons tend to get accumulated at the tip of the laser pulse, which may increase the local electron density at the laser pulse front.

3.3 3D-PIC Simulation Model

A circularly polarized laser propagating along Z direction of wavelength $\lambda = 1$ μm, normalized electric field amplitude $a_0 (= eE_0/m_e\omega c) \approx 10$ which corresponds to an intensity of 1.36×10^{20} W/cm^2, pulse duration $\tau = 30$ fs (FWHM) is incident on an overdense plasma target of density 1.15×10^{22} cm^{-3} ($10.32\ n_c$). Here, $n_c = m_e\omega^2/4\pi e^2$ is the critical density where e and m_e are the charge and mass of an electron respectively, ω is the laser frequency, E_0 is the laser electric field amplitude and c is the speed of light. The spot size of the laser pulse is 3 μm (FWHM) and the laser period

T_0 is 3.3 fs. A simulation box of dimensions 20 μm × 20 μm× 12 μm consisting of 200 × 200 × 120 cells has been used. The overdense plasma slab of height and width 10 μm and thickness 5 μm is sharply edged and is located at a distance of 2 μm from the left boundary of the simulation box as shown in Fig. 3.2. A vacuum gap

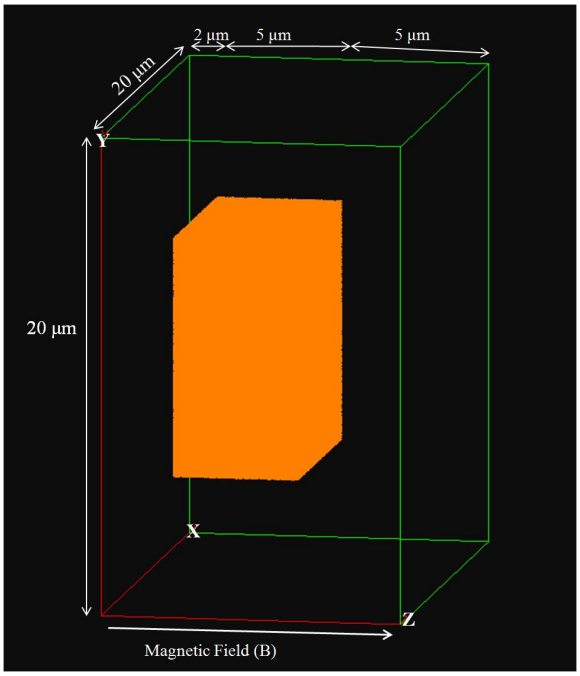

Fig. 3.2: 3D-PIC geometry of the simulation box.

of 5 μm is maintained across the rear side of target. A magnetic field of B = 50 MG ($\omega_{ce}/\omega \approx 0.5$) is applied along Z which is the axial direction. Absorbing boundary conditions have been incorporated along all the three directions. The simulations are done with 50 macroparticles per cell. The ions considered in these simulations are protons with mass $m_i = 1836\ m_e$. $\omega_{pe} = \sqrt{4\pi n_e e^2/m_e}$ and $\omega_{ce} = eB/m_e c$ are the electron plasma frequency and electron cyclotron frequency respectively where n_e is the electron plasma density. The plasma is initially assumed to be cold with $T_e = T_i = 0$ where T_e and T_i are the electron and ion temperatures respectively.

3.4 Acceleration in the presence of magnetic field

The high-intensity laser exerts high radiation pressure at the target front side and accelerates the protons via. RPA mechanism. The radiation pressure deforms the front surface of the target by pushing it inwards and the laser then behaves as if it is incident obliquely on the target. The laser then starts getting absorbed by vacuum

heating [19] which leads to the formation of sheath fields at the target front surface. These sheath fields cause the formation of microstructures which can penetrate the piston [20]. Thus, the hot energetic electrons are able reach the target rear side

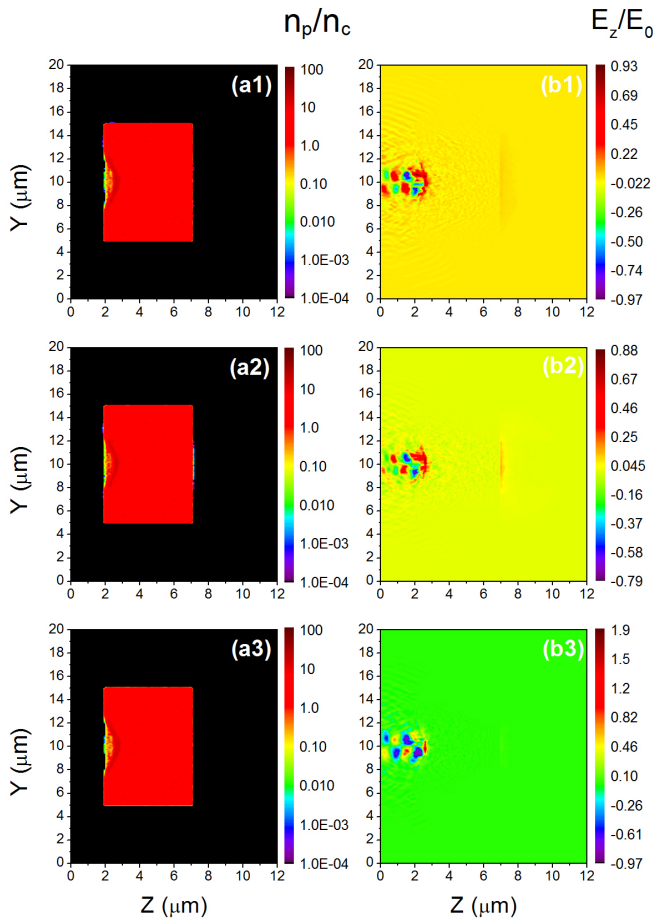

Fig. 3.3: Proton density distribution (a1-a3) and axial electric field (b1-b3) in the central YZ plane (X = 10 μm) at time 51 T_0 respectively for B = 0, RCP with B = 50 MG and LCP with B = 50 MG. The proton density n_p is normalized by the critical density $n_c = 1.12 \times 10^{21}$ cm^{-3} and the axial electric field E_z is normalized by the laser electric field E_0.

and accelerate the protons by the TNSA process. The formation and the motion of the laser piston can be observed clearly in Fig. 3.3 (a1), (a2) and (a3) which show the normalized proton density at time 51 T_0. In case of RCP, the direction of rotation of electrons by the laser electric field is same as the direction of gyration by the axial magnetic field, which enhances the effect of the laser ponderomotive force. Thus, the electrons become more energetic in case of RCP as shown in Fig. 3.4 (a) and as a result, they do not tend to remain in the electron sheath and move with high velocities towards the upstream plasma and accelerates protons on reaching the

target rear side as observed in Fig. 3.3 (a2). On the other hand, in case of LCP, the cyclotron effects get reversed as the direction of electron gyrations by the laser electric field and the axial magnetic field are opposite to each other which restricts electron motion and hence reduce electron energy as shown in Fig. 3.4 (a). As

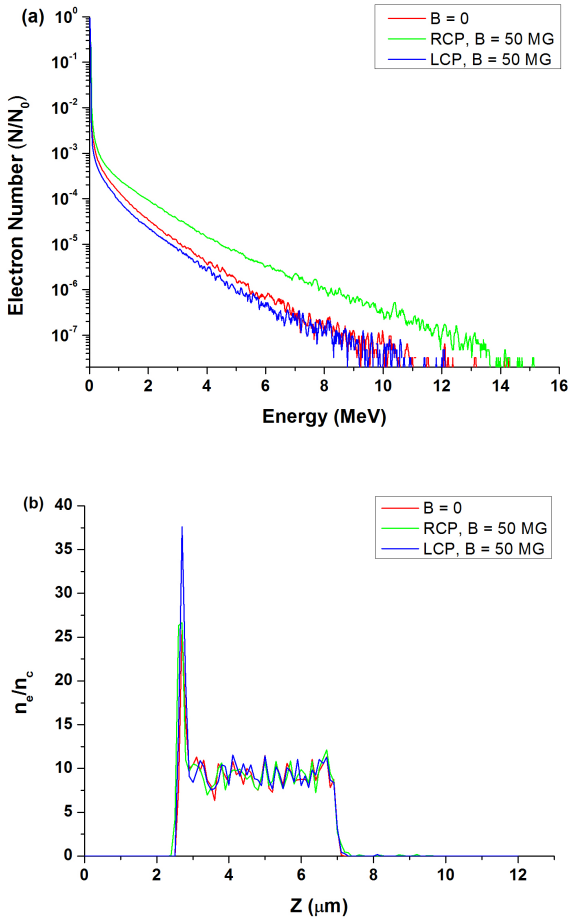

Fig. 3.4: (a) Electron energy spectrum (b) Electron density distribution along Z direction (X = 10 μm, Y = 10 μm) at time 51 T_0 for B = 0 (red solid), RCP with B = 50 MG (green solid) and LCP with B = 50 MG (blue solid). The electron density n_e is normalized by the critical density $n_c = 1.12 \times 10^{21}\text{cm}^{-3}$.

a result, the electrons get accumulated at the tip of laser pulse which causes an increase in local electron plasma density as shown in Fig. 3.4 (b). This electron accumulation strengthens the laser piston which decreases the transmitted laser field in the electron sheath. Hence, the laser ponderomotive force gets suppressed at a short distance which increases the radiation pressure. The magnitude of the electric field of the piston is about ≈ 2 times the fundamental laser electric field as observed in Fig. 3.3 (b3) which is comparatively higher than the other two cases as shown in Fig. 3.3 (b1) and (b2). Thus, at the initial stage, the protons get accelerated by

radiation pressure more effectively rather than by TNSA and hence generates more energetic protons at the target front side.

Fig. 3.5 (a), (b) and (c) show the normalized electron axial momentum (p_z/m_ec) phase space plots for the cases with B = 0, RCP and LCP in presence of magnetic field respectively. In case of RCP, it is observed that the flow of energetic electrons

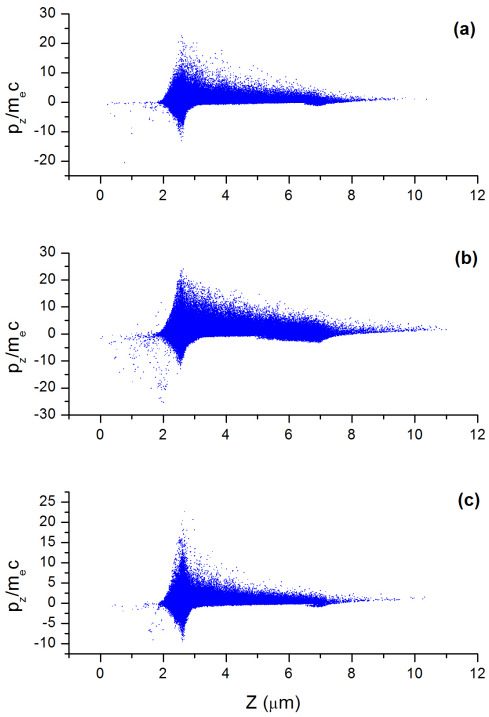

Fig. 3.5: Normalized electron axial momentum p_z/m_ec phase space for (a) B = 0, (b) RCP with B = 50 MG and (c) LCP with B = 50 MG at time 51 T_0.

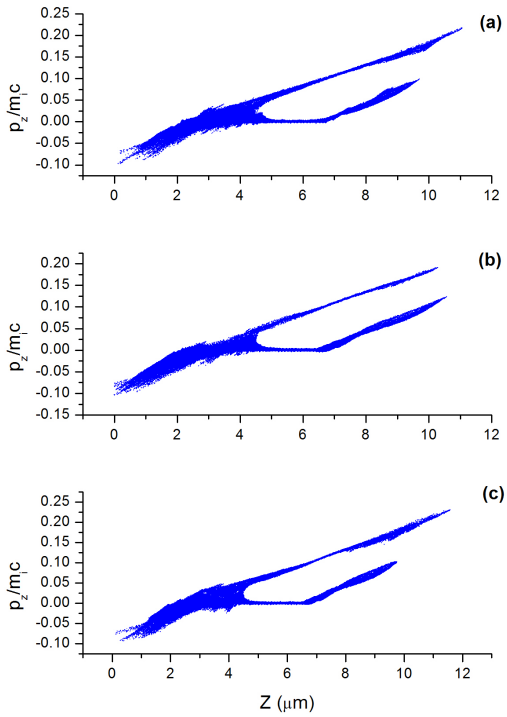

Fig. 3.6: Normalized proton axial momentum p_z/m_pc phase space for (a) B = 0, (b) RCP with B = 50 MG and (c) LCP with B = 50 MG at time 95 T_0.

towards the upstream plasma is comparatively higher in number than the cases with B = 0 and LCP. However, in case of LCP, a comparatively sharper peak at Z ≈ 2.3 μm show that the energetic electrons get confined at a short distance due to cyclotron effects. This leads to a strong charge separation region which accelerates the protons from the target front side more effectively as compared to the other two cases. Hence, the protons accelerated by the LCP laser pulse in presence of magnetic field are more energetic as compared with the other two cases. Fig. 3.6 (a), (b) and (c) show the normalized proton axial momentum (p_z/m_pc) phase space plots for the cases with B = 0, RCP and LCP in presence of magnetic field respectively at time 95 T_0. It can be observed that, the protons accelerated from the target front side

by the radiation pressure of LCP laser pulse in presence of magnetic field gain more energy and travel faster as compared to those with RCP and B = 0. The direction of

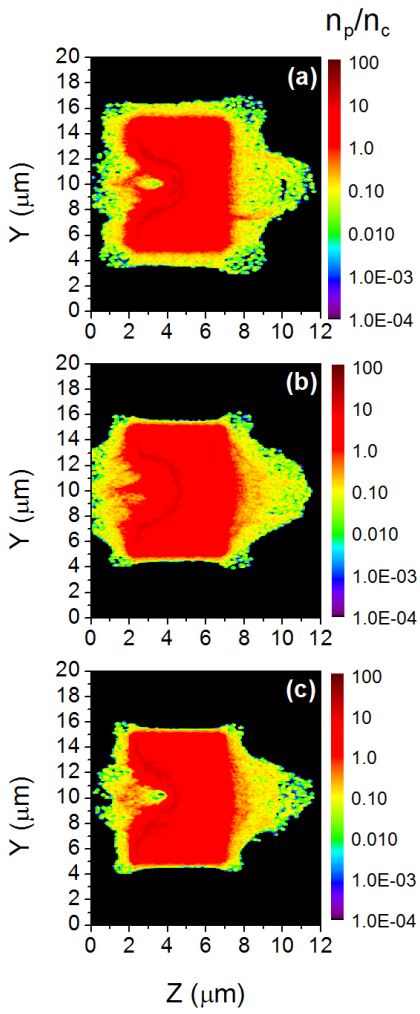

Fig. 3.7: Proton density distribution in the central YZ plane (X = 10 μm) for (a) B = 0 at time 98 T_0, (b) RCP with B = 50 MG at time 101 T_0 and (c) LCP with B = 50 MG at time 95 T_0. The proton density n_p is normalized by the critical density $n_c = 1.12 \times 10^{21}\text{cm}^{-3}$.

proton gyrations and the rotation of electric field vector is same in case of LCP and opposite in case RCP which may also contribute towards the gain and decrease in proton energy respectively. However, in case of RCP, it can be observed from Fig. 3.6 (b) that the energy gained by the protons at the target rear side via TNSA process is comparatively higher as compared to those with LCP and B = 0 and they travel a distance at the target rear side almost equal to the distance travelled by the protons accelerated due to the radiation pressure. Thus, it can be concluded that a RCP laser pulse in presence of magnetic field favours TNSA and the TNSA accelerated protons

although lower in energy, travel along with the radiation pressure accelerated protons at the target rear side. Fig. 3.7 (a), (b) and (c) represents the normalized proton density for B = 0, RCP and LCP at times 98 T_0, 101 T_0 and 95 T_0 respectively. It can be observed that the energetic protons travel an equal distance of $\approx 5\mu m$ from the target rear side at different times. The highest amount of time is taken in case of an RCP laser pulse due to low energy gain as shown in Fig. 3.8. It can also be

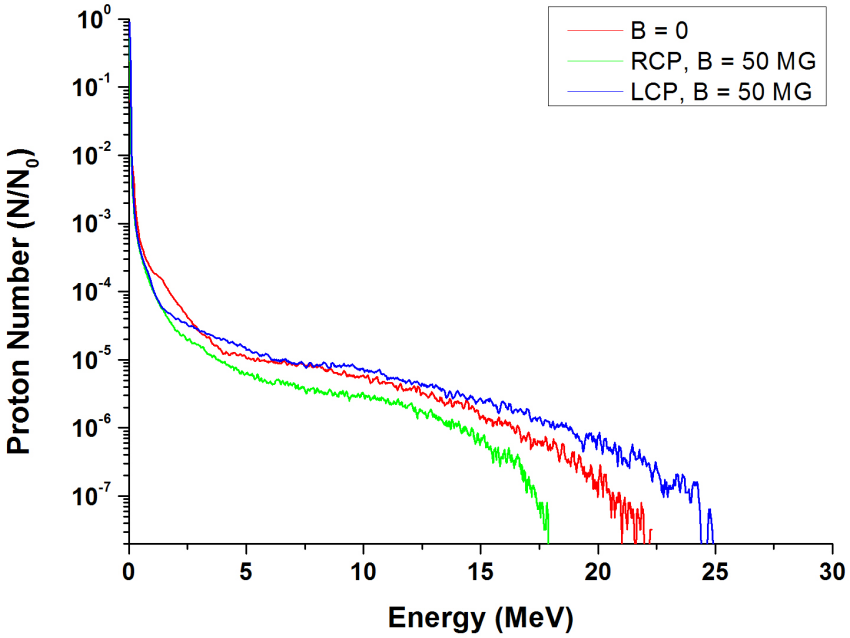

Fig. 3.8: Proton energy spectrum for B = 0 (red solid) at time 98 T_0, RCP with B = 50 MG (green solid) at time 101 T_0 and LCP with B = 50 MG at time 95 T_0 (blue solid).

observed from Fig. 3.7 that the transverse motion of protons is considerably reduced due to cyclotron effects as the protons gyrate around the axial magnetic field which restricts the transverse motion. However, the protons get accelerated more along the backward direction from the target front surface due to sheath fields in case of RCP whereas this backward acceleration is observed to be reduced in case of LCP. The protons gain a maximum energy of 25 MeV in case of LCP and 18 MeV in case of RCP. Thus, the energy gain is highest for an LCP laser pulse which is in agreement with the results obtained by Sharma et al. [17]. Fig. 3.9 shows the proton density in the XY plane (Z = 11 μm) at times when the energetic protons have traversed a distance of $\approx 5\mu m$ from the rear side of the target in all the three cases. It can be observed that the proton beams at the rear side have a smaller spot size and hence

are comparatively more collimated in case of LCP laser pulse. The collimation is less in case of RCP.

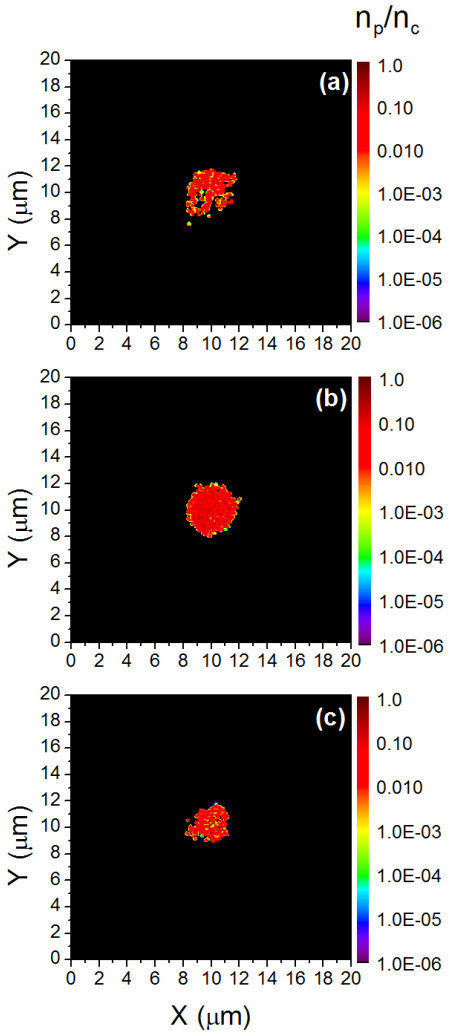

Fig. 3.9: Proton density distribution in the XY plane (Z = 11 μm) for (a) B = 0 at time 98 T_0, (b) RCP with B = 50 MG at time 101 T_0 and (c) LCP with B = 50 MG at time 95 T_0. The proton density n_p is normalized by the critical density $n_c = 1.12 \times 10^{21}\text{cm}^{-3}$.

The simulations are repeated for targets with different thicknesses in order to find the optimum thickness at which the energy gain would be maximum. In absence of magnetic field, the optimum thickness at which the protons gain maximum energy is found out to be $0.6\mu m$. In presence of magnetic field, the optimum thickness is found out to be $0.7\mu m$. However, the maximum energy for LCP is more than RCP as shown in Fig. 3.10. Thus, it can be concluded that the optimum thickness gets increased in presence of an axial magnetic field which is mainly due to the cyclotron effects that modifies the ponderomotive action of the laser pulse.

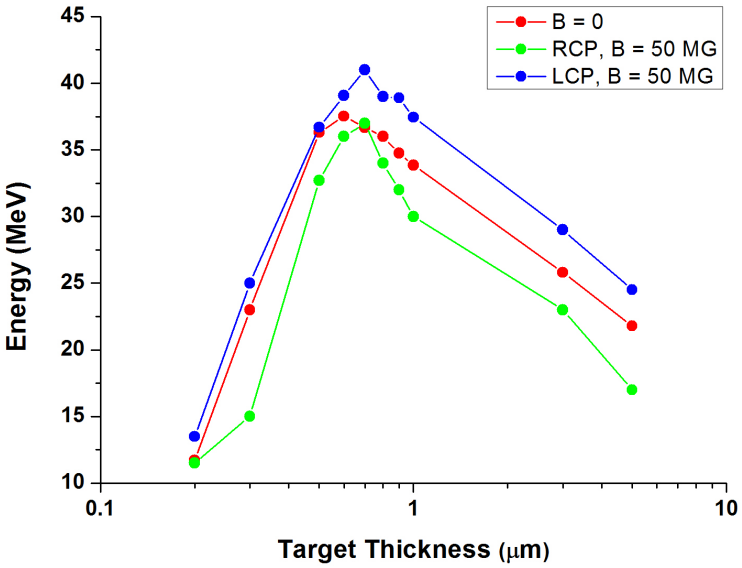

Fig. 3.10: Variation of maximum proton energy with target thickness for for B = 0 (red solid), RCP with B = 50 MG (green solid) and LCP with B = 50 MG (blue solid).

Acceleration at moderate laser intensity:

The radiation pressure becomes dominant when the laser is highly intense. Since, TNSA is also observed to play an important role in the acceleration process in addition to RPA in our case and RCP in presence of an axial magnetic field is observed to favour TNSA, we repeated the simulations with a moderately intense laser in order to make RPA less effective. This would help us to observe the cyclotron effects mainly on TNSA induced by a circularly polarized laser. The simulations are repeated for all the cases by reducing the laser intensity to 10^{19} W/cm^2 ($a_0 \approx 2.8$) whereas all the other parameters remain same. It can be observed from the normalized electron density plots as shown in Fig. 3.11 (c) that the target front surface gets bent inward and the electron density rises more sharply in case of a LCP laser as compared to the other two cases in Fig. 3.11 (a) and (b). It is also observed that the axial magnetic field considerably reduces the transverse electron motion due to cyclotron effects which improves the beam collimation. Fig. 3.12 shows the normalized proton axial momentum (p_z/m_ic) phase space plots for all the three cases at different times. It can be observed, that for a RCP laser, the protons gain highest momentum at the target rear side at time 60 T_0 whereas that for a LCP laser is lowest. On the other hand, the protons gain highest momentum in case of LCP laser and lowest

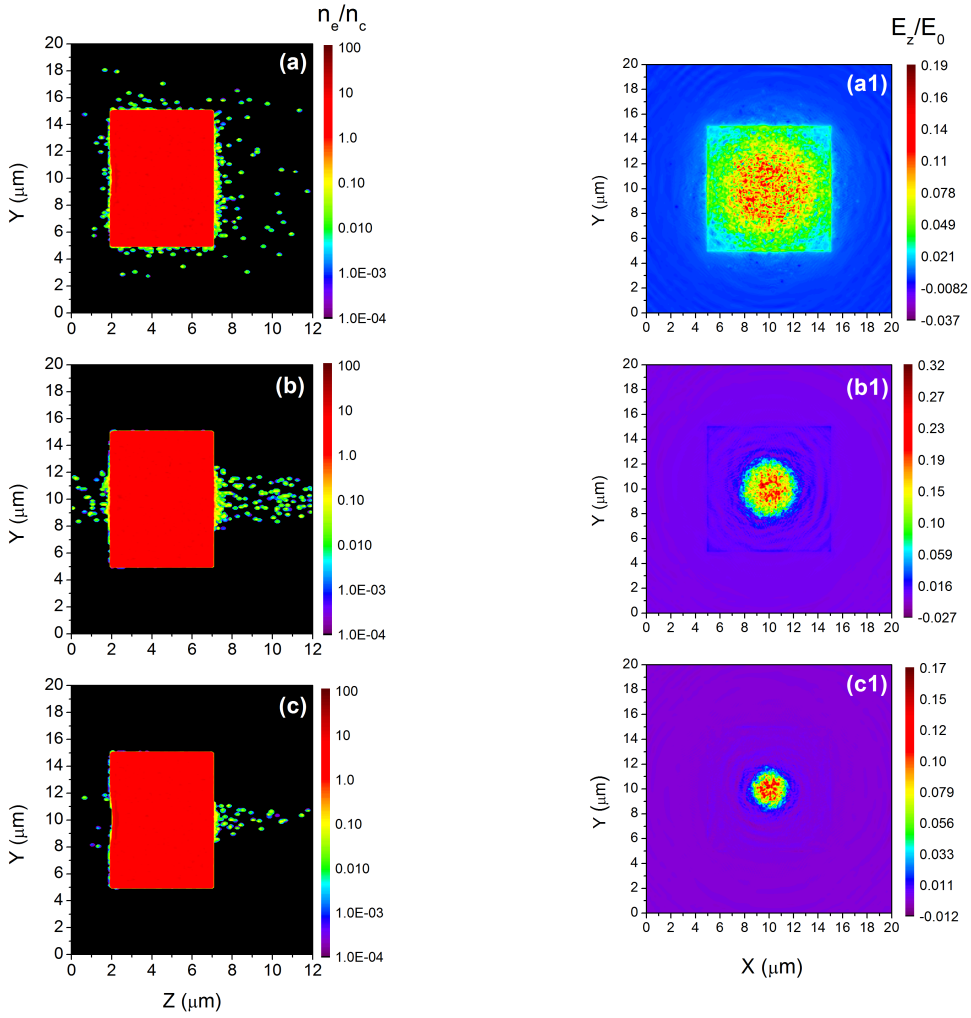

Fig. 3.11: Electron density distribution (a-c) in the central YZ plane (X = 10 μm) and axial electric field (a1-c1) in the XY plane (Z = 7 μm) at time 60 T_0 respectively for B = 0, RCP with B = 50 MG and LCP with B = 50 MG. The electron density n_e is normalized by the critical density $n_c = 1.12 \times 10^{21}$cm^{-3} and the axial electric field E_z is normalized by the laser electric field E_0.

momentum in case of RCP laser at the target front side. At the initial stage of acceleration, the protons get accelerated more effectively from the target front side and the energy obtained is highest in case of LCP laser due to the dominant effect of radiation pressure. But, as the laser is moderately intense, the radiation pressure effect decreases with time. With the passage of time, the hot electrons reach the target rear surface and accelerate protons via. TNSA up to high energies than those accelerated due to radiation pressure effect. Thus, at the initial stage of acceleration, LCP laser produces high energetic protons but at a later stage, the energy obtained from a RCP laser is highest as shown in Fig. 3.13. When the laser is ultra intense, the energy obtained by LCP laser is highest due to dominant radiation pressure effect

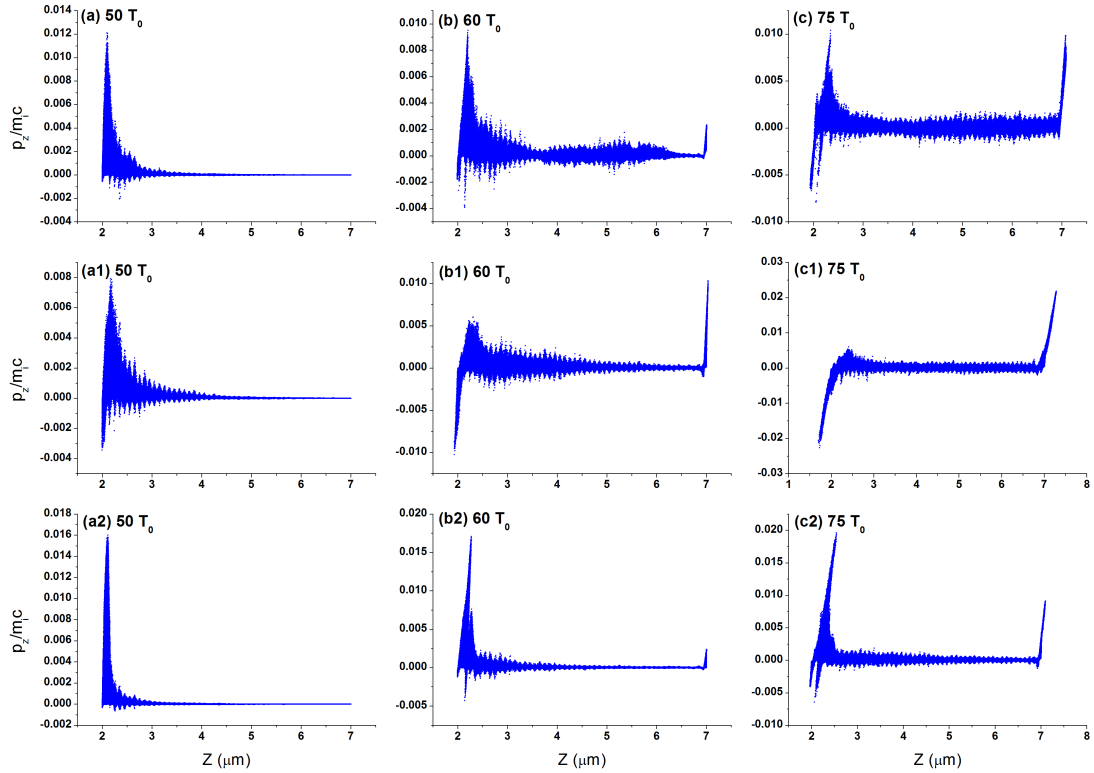

Fig. 3.12: Normalized proton axial momentum p_z/m_ic vs Z (μm) phase space for B = 0 (a,b and c), RCP with B = 50 MG (a1,b1 and c1), LCP with B = 50 MG (a2,b2 and c2) at times 50 T_0, 60 T_0 and 75 T_0 respectively.

and the radiation pressure accelerated protons generated from the target front side reach the target rear side. In case of a moderately intense laser, the effect of radiation pressure is weak and hence, it ceases with time. The flow of hot electrons across the target rear side increases with time gradually and so the rear side acceleration produces highest energetic protons. Since, RCP laser favours rear side acceleration, the energy obtained by a RCP laser is highest in this case.

3.5 Conclusion

The effect of an axial magnetic field in generating high energetic protons from an overdense plasma target by an ultraintense short pulse circularly polarized laser has been investigated with the help of 3D-PIC simulations. The conclusions drawn from the above discussions can be summarized as follows:

i) The laser ponderomotive force gets enhanced by an axial magnetic field in case of RCP due to cyclotron effects and hence generate more energetic electrons

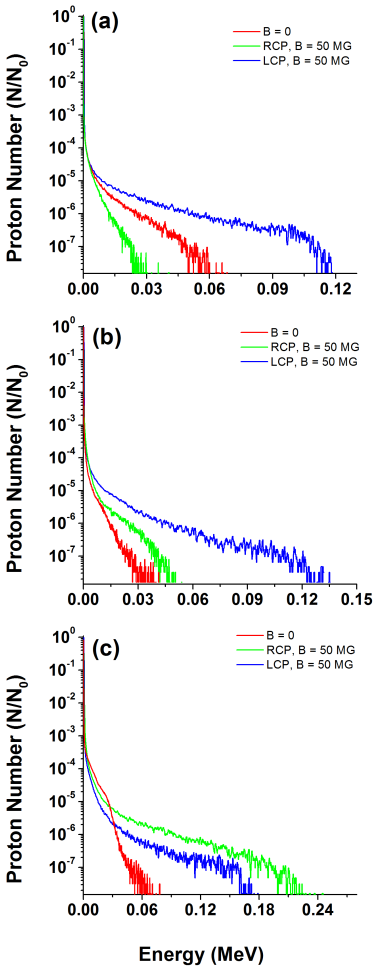

Fig. 3.13: Proton energy spectrum at (a) 50 T_0, (b) 60 T_0 and (c) 75 T_0 for B = 0 (red solid), RCP with B = 50 MG (green solid) and LCP with B = 50 MG (blue solid).

which leave the electron sheath and travel through the upstream plasma and on reaching the target rear side accelerates protons via TNSA process. Whereas in case of LCP the electrons get more accumulated in the electron sheath which increases the radiation pressure and accelerates protons more effectively to higher energies from target front side.

ii) An axial magnetic field favours TNSA in case of RCP whereas protons are accelerated more effectively by the radiation pressure in case of LCP.

iii) The transverse motion of the protons get reduced in presence of an axial magnetic field due to cyclotron effects.

iv) The protons accelerated by the LCP laser pulse in presence of axial magnetic

field has highest collimation and hence have a comparatively smaller spot size.

v) The maximum proton energy obtained is higher for LCP and lower for RCP in presence of an axial magnetic field as compared to the energy obtained in absence of magnetic field.

vi) The optimum thickness of the target at which the energy gain is maximum increases slightly in presence of an axial magnetic field both for RCP and LCP laser pulses. However, the maximum energy obtained at optimum thickness is still higher for LCP laser pulse.

vii) In case of a moderately intense laser, as the radiation pressure effect is weak, it ceases with time. The hot electron flow across the target rear side increases with time gradually which enhances the rear side acceleration producing high energetic protons. As RCP favours rear side acceleration, maximum proton energy obtained by a RCP laser is observed to be highest in this case.

Bibliography

[1] Debray, F. and Frings, P. State of the art and developments of high field magnets at the laboratoire national des champs magntiques intenses. *Comptes Rendus Physique*, 14(1):2 – 14, 2013. Physics in High Magnetic Fields / Physique en champ magntique intense.

[2] Sims, J. R., Rickel, D. G., Swenson, C. A., Schillig, J. B., Ellis, G. W., and Ammerman, C. N. Assembly, commissioning and operation of the nhmfl 100 tesla multi-pulse magnet system. *IEEE Transactions on Applied Superconductivity*, 18(2):587–591, 2008.

[3] Schmit, P. F., Knapp, P. F., Hansen, S. B., Gomez, M. R., Hahn, K. D., Sinars, D. B., Peterson, K. J., Slutz, S. A., Sefkow, A. B., Awe, T. J., Harding, E., Jennings, C. A., Chandler, G. A., Cooper, G. W., Cuneo, M. E., Geissel, M., Harvey-Thompson, A. J., Herrmann, M. C., Hess, M. H., Johns, O., Lamppa, D. C., Martin, M. R., McBride, R. D., Porter, J. L., Robertson, G. K., Rochau, G. A., Rovang, D. C., Ruiz, C. L., Savage, M. E., Smith, I. C., Stygar, W. A., and Vesey, R. A. Understanding fuel magnetization and mix using secondary nuclear reactions in magneto-inertial fusion. *Phys. Rev. Lett.*, 113:155004, 2014.

[4] Tatarakis, M., Watts, I., Beg, F. N., Clark, E. L., Dangor, A. E., Gopal, A., Haines, M. G., Norreys, P. A., Wagner, U., Wei, M.-S., Zepf, M., and Krushelnick, K. Measuring huge magnetic fields. *Nature*, 415:280, 2002.

[5] Wilks, S. C., Kruer, W. L., Tabak, M., and Langdon, A. B. Absorption of ultra-intense laser pulses. *Phys. Rev. Lett.*, 69:1383–1386, 1992.

[6] Sandhu, A. S., Dharmadhikari, A. K., Rajeev, P. P., Kumar, G. R., Sengupta, S., Das, A., and Kaw, P. K. Laser-generated ultrashort multimegagauss magnetic pulses in plasmas. *Phys. Rev. Lett.*, 89:225002, 2002.

[7] Mondal, S., Narayanan, V., Ding, W. J., Lad, A. D., Hao, B., Ahmad, S., Wang, W. M., Sheng, Z. M., Sengupta, S., Kaw, P., Das, A., and Kumar, G. R. Direct observation of turbulent magnetic fields in hot, dense laser produced plasmas. *Proceedings of the National Academy of Sciences*, 109(21):8011–8015, 2012.

[8] Fujioka, S., Zhang, Z., Ishihara, K., Shigemori, K., Hironaka, Y., Johzaki, T., Sunahara, A., Yamamoto, N., Nakashima, H., Watanabe, T., Shiraga, H., Nishimura, H., and Azechi, H. Kilotesla magnetic field due to a capacitor-coil target driven by high power laser. *Scientific Reports*, 3:1170, 2013.

[9] Santos, J. J., Bailly-Grandvaux, M., Giuffrida, L., Forestier-Colleoni, P., Fujioka, S., Zhang, Z., Korneev, P., Bouillaud, R., Dorard, S., Batani, D., Chevrot, M., Cross, J. E., Crowston, R., Dubois, J.-L., Gazave, J., Gregori, G., dHumires, E., Hulin, S., Ishihara, K., Kojima, S., Loyez, E., Marqus, J.-R., Morace, A., Nicola, P., Peyrusse, O., Poy, A., Raffestin, D., Ribolzi, J., Roth, M., Schaumann, G., Serres, F., Tikhonchuk, V. T., Vacar, P., and Woolsey, N. Laser-driven platform for generation and characterization of strong quasi-static magnetic fields. *New Journal of Physics*, 17(8):083051, 2015.

[10] Wang, W.-M., Gibbon, P., Sheng, Z.-M., and Li, Y.-T. Magnetically assisted fast ignition. *Phys. Rev. Lett.*, 114:015001, 2015.

[11] Hosokai, T., Kinoshita, K., Zhidkov, A., Maekawa, A., Yamazaki, A., and Uesaka, M. Effect of external static magnetic field on the emittance and total charge of electron beams generated by laser-wakefield acceleration. *Phys. Rev. Lett.*, 97:075004, 2006.

[12] Farina, D., Lontano, M., and Bulanov, S. Relativistic solitons in magnetized plasmas. *Phys. Rev. E*, 62:4146–4151, 2000.

[13] Borhanian, J., Kourakis, I., and Sobhanian, S. Electromagnetic envelope solitons in magnetized plasma. *Physics Letters A*, 373(40):3667 – 3677, 2009.

[14] Feng, W., Li, J. Q., and Kishimoto, Y. Relativistic soliton formation in laser magnetized plasma interactions. *Journal of Physics: Conference Series*, 717(1): 012031, 2016.

[15] Bulanov, S. V., Esirkepov, T. Z., Kando, M., Koga, J. K., Hosokai, T., Zhidkov, A. G., and Kodama, R. Nonlinear plasma wave in magnetized plasmas. *Physics of Plasmas*, 20(8):083113, 2013.

[16] Sharma, A. and Tripathi, V. Relativistic and ponderomotive self-focusing of a laser pulse in magnetized plasma. *Laser and Particle Beams*, 30(4):659664, 2012.

[17] Sharma, A., Liu, C. S., and Tripathi, V. K. Cyclotron effects on double layer ion acceleration from laser-irradiated thin foils. *Physics of Plasmas*, 17(1):013101, 2010.

[18] Upadhyay, A., Patel, K., Rao, B. S., Naik, P. A., and Gupta, P. D. Three-dimensional simulation of laser–plasma-based electron acceleration. *Pramana*, 78(4):613–623, 2012.

[19] Brunel, F. Not-so-resonant, resonant absorption. *Phys. Rev. Lett.*, 59:52–55, 1987.

[20] Chen, M., Pukhov, A., Sheng, Z. M., and Yan, X. Q. Laser mode effects on the ion acceleration during circularly polarized laser pulse interaction with foil targets. *Physics of Plasmas*, 15(11):113103, 2008.